Neutron radiography and current distribution measurements for studying the influence of the cathode flow field properties on the water distribution and performance of direct methanol fuel cells

A. Schröder[a], K. Wippermann[a*], T. Arlt[b], T. Sanders[c], T. Baumhöfer[c], N. Kardjilov[b], A. Hilger[b], J. Mergel[a], W. Lehnert[a], D. Stolten[a,d], J. Banhart[b], I. Manke[b]

[a]Institute of Energy and Climate Research, IEK-3: Fuel Cells, Forschungszentrum Jülich GmbH, 52425 Jülich, Germany

[b]Helmholtz-Zentrum Berlin, Institute for Applied Materials, Hahn-Meitner-Platz 1, 14109 Berlin, Germany

[c]Institute for Power Electronics and Electrical Drives (ISEA), RWTH Aachen University, Jägerstraße 17–19, 52066 Aachen, Germany

[d]Chair for Fuel Cells, RWTH Aachen University, Germany

*corresponding author; tel.: +49 2461 61 2572; fax: +49 2461 61 6695; e-mail address: k.wippermann@fz-juelich.de

Keywords: DMFC stack cell; neutron radiography; spatially/ temporally resolved current density; hydrophilic/hydrophobic surface properties; cathode flow field design

Summary

The influence of the cathode flow field properties on the water distribution and performance of direct methanol fuel cells (DMFCs) was studied. All measurements were performed with DMFC stack cells (A = 314.75 cm²). The local and temporal water distributions in the flow field channels during DMFC operation were visualized by means of through-plane neutron radiography. Current and temperature distributions were measured simultaneously by the segmented cell technology. Additionally, the time-dependent current distribution, cell performance and pressure drop were measured. Cathode flow field designs with channel and grid structures were compared. The cathode flow field channels were either impregnated by hydrophobizing or hydrophilizing agents or used as received. It turned out that hydrophobized and partially also untreated flow fields cause large water droplets in the cathode channels. The water droplets cause a blocking of the air flow and consequently a lower and more unstable (fluctuating) performance, less steady current and temperature distributions and higher pressure drops between cathode inlet and outlet. Because of their two-dimensional design, grid flow fields are less prone to water accumulations. The best results are achieved with a hydrophilized grid flow field which has a channel depth and width of 1.5 mm each (‘C-GR15’).

1. Introduction

In direct methanol fuel cells (DMFCs), the amount of water on the cathode side is considerably higher than in hydrogen-powered polymer electrolyte fuel cells (PEFCs). Not only does the product water accumulate, but additional water and methanol permeate from the anode through the membrane to the cathode. A part of the water evaporates and is carried away by the flowing gas. The remaining liquid water is transported through the pores of the catalyst and

diffusion layer until it reaches the flow field channels and from there, it is also removed by the air flow.

Unfavorable wetting properties and flow conditions can cause flooding in the functional layers and flow channels that can complicate the oxygen transport and prevent a stable cell operation [1-9]. In the literature, the impact of various surface properties on droplet movement and water transport are discussed [7, 10-17]. Similar to rough surfaces, micro-structured surfaces can exhibit a wicking effect whose degree of intensity depends on the design [11]. Droplets with a larger contact angle offer a larger cross-sectional area than droplets with a smaller contact angle and, for this reason, films can be moved more easily. However, larger contact angles resulting from a hydrophobic gas diffusion layer (GDL) have a positive effect at high air ratios only [13]. According to Ref. [14], while channels with hydrophobic coating contain more water in total, the accumulations are more numerous and smaller and permit a better cell performance at high current densities. According to Ref. [15], a hydrophobic land area of the flow field favors water transport from the GDL. In the same way, hydrophilic channel surfaces cause lower accumulations of water within the GDL [16]. In both cases, the improved water removal can be attributed to different degrees of wettability in the channels and below the lands because on surfaces with a gradient of wettability droplets can move from hydrophobic to hydrophilic even against gravity [17]. One of our recent studies revealed that especially at low air stoichiometry ($\lambda_{air} = 2$) hydrophilic cathode flow fields are advantageous with regard to higher power densities, the suppression of local current fluctuations and the substantial reduction of the pressure drop along the cathode channels [8].

Owing to the high sensitivity of neutron radiation to hydrogen-rich compounds, neutron radiography is a suitable method for studying water accumulations in fuel cells and is now an established technique in the area of PEFCs [18-23] Using radiography, the water layer thickness in the direction of

the beam can only be detected two-dimensionally. This is why two different viewing directions are used: The neutron radiation hits the measuring cell either from the front (through-plane) [24-26] or from the side (cross-section) [19, 27-31].

The through-plane viewing direction provides an overview over the entire electrode surface [25, 26, 30, 32-47]. The impact of operating parameters, material and flow field geometry on the water distribution and performance properties can be studied. For surface areas up to 100 cm^2, the spatial resolution usually ranges between 100 µm and 250 µm. Dynamic processes can also be tracked to a limited extent with exposure times between 10 s and 30 s. If the geometries of the anode and cathode channels differ such that they are not or are only slightly superimposed in the projection, a distinction can be made between liquid water in the channels of the anode and cathode side [34]. In combination with simultaneous optical observation by means of transparent flow fields, information can also be obtained about the fraction of water in the layers of the MEA [40]. If at the same time the current density distribution is measured via the electrode surface this can be correlated with the water distribution [26]. Vertical separation can be used to directly compare the effects of different material properties on the water distribution. This means that it is possible, for example, to analyze two different diffusion layers next to each other [45].

Previous studies on DMFCs were limited to the impact of the flow velocity and direction on the accumulation of carbon dioxide in the anode channels [48-50].

In spite of its restrictions with respect to availability and temporal and spatial resolution, neutron radiography has a number of advantages. As in PEFCs, the fluid distribution in DMFCs can be analyzed in largely unmodified common cells during operation. Doing this, it is possible to either view entire electrode surfaces in the through-plane viewing direction or study processes in

individual MEA layers and flow field channels in a cross-sectional viewing direction. A combination of neutron radiography with current density measurements permits a correlation to be drawn between liquid distribution and current density distribution and is especially promising [7, 8].

The goal of this work is to use combined neutron radiography and spatially resolved current density measurements for studying the influence of hydrophilic and hydrophobic properties of cathode flow fields in large DMFC stack cells on the water distribution and water discharge in the cathode flow field channels, the cell performance and temporal fluctuations of performance. A cell design and neutron radiography set-up is presented which allows for a simultaneous investigation of complete, large stack cells ($A \approx 315$ cm²) by neutron radiography and spatially resolved current density measurements.

2. Experimental

2.1. Cell design

The cell design used for this experiment offers the opportunity to reproduce the operations of a stack single cell of the horizontal order picker (a type of forklift) which is powered by a DMFC system developed at Forschungszentrum Jülich [51, 52]. The geometry and materials of the flow fields correspond to the components of the stack. This is also true for the two frames made of fiberglass-reinforced plastic. The area ($A = 314.75$ cm^2) and shape of the electrodes are also identical. The flow fields mentioned above consist of a 1.5-mm thick layer of binder-free Sigraflex (expanded graphite, SGL Group) in which the channels are embedded at full depth. The channel structures are pressed with a 0.55-mm thick back wall made of impregnated Sigraflex to keep the channels dimensionally stable. The design and specific properties of the flow fields used in this work are shown in Table 1 and Figure 1. The anode structure (see Figure 1, upper left) consists of a total of six 1.5-

mm wide meandering channels. In each case, three channels have a common inlet and supply one half of the cell. Similar to the stack, the methanol solution is admitted via the end plates and fed into the channels from the side. The cathode structure (see Figure 1, upper right) consists of straight parallel channels, which are also 1.5-mm wide. In addition to the channel structure, two flow fields with a grid structure are also used on the cathode side. The edge lengths of the cubes and distances between the cubes are either 1.0 mm (lower left) or 1.5 mm (lower right). Increasing the edge lengths and distances between the cubes causes the flow velocity to drop. To ensure stability, requires the thickness of the plate to be increased to 4 mm instead of 3 mm. Since unlike the channel structures grid structures cannot be installed in the flow field plate at full depth, the corresponding flow fields are manufactured in a single piece using graphite instead of Sigraflex. This eliminates the need for an additional back wall splitter. The end plates made of gold-plated aluminum are fabricated with a thickness of 20 mm and fitted with four heating cartridges each. The boreholes required for the set-up are arranged above and below outside the beam path.

Place Table 1 here

Place Figure 1 here

Air is supplied from above over the entire width of the channel surface. Recesses above and below in the back wall, the seals and in the anode flow field form an adjacent gap through which the air can flow in and out. For cathode flow fields with channel structure, an absorbent wick is inserted into the recess of the back wall in order to make it easier for water droplets to drain off from the channel ends. The wick absorbs water from the channels and

allows it to drop off below. For cathodes flow fields with grid structure, wicks are not required.

For the segmented derivation of the current, a printed circuit board (PCB) is used that has 54 contact segments adapted to the shape of the electrode surface, along with the same number of temperature sensors (Figure 2). To protect the set-up from moisture, a 0.5-mm thick baffle plate made of Sigraflex is inserted between the cathode flow field and the (PCB). The arrangement of the cell components is shown in Figure 3. For the sake of simplicity, the temperature sensors on the back of the PCB are not shown.

Place Figure 2 here

Place Figure 3 here

2.2. Flow field treatment

The surfaces of the flow fields were treated with different substances in order to vary the contact angle of water. Two different materials were used for the flow field fabrication: BBP4 [53] and Sigraflex [54] (expanded graphite of the SGL Group). The resulting contact angles are given in Table 2.

.

Place Table 2 here

In case of the stack MEAs used for combined neutron radiography and current distribution measurements, the channels in the left half of the flow fields were either hydrophobized or hydrophilized, whereas the channels in the right half of the flow fields remained untreated (as-received). In the current distribution

experiments without neutron radiography, the full cathode channel area of the flow fields was either hydrophobized, hydrophilized or remained as-received.

2.3. MEA Preparation

As a substrate for the anodes and cathodes, AvCarb 1071 HCB carbon cloth supplied by Ballard Material Products was used. In the first step, it was impregnated with PTFE dispersion TF 5032 supplied by Dyneon and subsequently dried and sintered at 350°C. First, a microporous layer of carbon particles and PTFE was applied to the cloth. The carbon particles and the PTFE are from the products VULCAN XC72 from Cabot and TF 5032 from Dyneon. In a second coating step, the catalyst layers were applied. Both catalyst layers consisted of catalyst material from Johnson Matthey and Nafion®. In case of the cathode catalyst layer, PTFE was added too. The starting materials of PTFE and Nafion® are the PTFE dispersion TF 5032 from Dyneon and the Nafion® dispersion LQ1115 from Ion Power. As catalyst material for the cathode, Johnson Matthey HiSPEC® 13100 (71 % wtPt/C) was used, while Johnson Matthey HiSPEC® 12100 (75 wt% PtRu/C) was used as the anode catalyst. The catalyst loadings were between 1.8 and 2.7 mg Pt/cm² in the cathodes and between 1.7 and 2.5 mg PtRu/cm^2 in the anodes. After the catalyst layer had dried, it was manually sprayed with Nafion® dispersion LQ1115 manufactured by Ion Power. Finally, the anodes and cathodes were shaped as desired and pressed into finished MEAs for three minutes at a temperature of 130°C and a pressure of 500 N/cm² with an N115 Nafion® membrane manufactured by DuPont.

2.4. Neutron radiography

The neutron source BERII at Helmholtz-Zentrum Berlin, Germany was used for the radiographic measurements. A versatile radiography set-up is allocated

at the station CONRAD (COld Neutron RADiography) [55, 56]. As shown in Figure 4, the neutrons have to pass a curved neutron guide to arrive at the experiment. The neutron source emits both γ radiation and neutrons, but only slow neutrons are able to follow the curvature of the guide. The γ radiation and also fast neutrons will be absorbed by the radiation protection close to the neutron guide. Approximately 10^7 neutrons / s^{-1} cm^2 arrive at the experiment and the background of undesired radiation is very low.

Place Figure 4 here

The spatial resolution depends on the L/D ratio, the applied magnification of the optical system and the dimensions of the pixels of the CCD camera. The opening of the aperture was set to 30 mm, which results in a L/D ratio of about 170. The spatial resolution was optimized by moving the fuel cell as close as possible to the 400-µm thick ^{6}LiF-ZnS scintillator [57, 58]. The exposure time per radiographic image was t = 10 s. The CCD chip of the DW436 camera from Andor Technologies [59] (2048 × 2048 pixels) was cooled down to –50°C ± 2K to limit thermal noise. The pixel resolution was 100 µm and the achieved physical spatial resolution about 200 µm over an area of 200 × 200 mm^2. To prevent radiation damage of the CCD chip a mirror was used to deflect the visible light by an angle of 90°. Additional radiation protection shieldings were installed around the camera box.

The fuel cell was fixed on a rotation table which was positioned on a translation stage. Therewith, the cell could be moved out of the beam in order to measure the open beam for normalization purposes. Further, an exact positioning of the cell with respect to the neutron beam was possible.

The electrode surface of stack cells cannot be completely illuminated with the usual set-up that has a limited beam size of about 100 × 100 mm^2. Although it

would be possible to measure the cell sequentially by shifting it within the beam, this would require more time and make data evaluation more complex [60]. A simultaneous investigation of the entire cell could only be performed if the neutron beam cross section was expanded. By applying a special technique instead of using a simple aperture between the outlet of the neutron guide and the measuring cell, the radiation cone can be widened both in the horizontal and vertical directions. This technique involves using an elliptically shaped neutron guide that first focuses the neutron radiation through reflection, after which behind the focus the radiation diverges [61]. Figure 5 shows the resulting beam profile with a maximum intensity located in the middle of the radiograph. Above and below as well as beside this maximum a decrease of the intensity was measured. The corners are illuminated almost inadequately. The right image in Figure 5 shows the same radiograph as the left image with an adapted contrast in order to show the intensity distribution in the area of maximum intensity. In line with the distribution of intensity, a location-dependent quality of the neutron radiographs results due to the varying signal-to-noise-ratios. For this reason, only a qualitative interpretation of the fluid distribution is possible.

Place Figure 5 here

2.5. Electrochemical measurements

The spatially resolved current density measurements were performed with a custom-designed multi-channel measurement device named EIScell developed by ISEA (RWTH Aachen University). The EIScell has 108 measuring channels that can be used to measure the currents and voltages of 54 segments simultaneously. The measurement principle is based on a PCB for contacting and an electronic circuit to form an equipotential surface. The overall current

strength is controlled digitally. The maximum segment strength of 2.5 A permits measurements to be performed with all cell designs used. Further information on the EIScell can be found in Ref. [62].

In order to record the temperature distribution, type DS18B20U digital sensors from Maxim Integrated Products are used [63]. The sensors on the back of a PCB are connected with a bus system; each sensor can be unambiguously identified via a unique code. With an increment of 0.0625°C, temperatures between − 55°C and + 125°C can be measured. The measurement error in the relevant temperature range is a maximum of ± 0.5°C.

A differential pressure sensor based on the MPX5010DP analogue pressure sensor [64] is used to measure the difference in pressure between the cathode inlet and outlet. In the pressure range between 0 mbar and 100 mbar the differential pressure can be measured with a resolution of about 0.1 mbar. The signal to noise ratio was found to be good enough to distinguish pressure variations as low as 1 mbar from the noise floor, making the device suitable for the detection of very low differential pressure variations. The measuring cell is mounted on a base plate; the end plates are not permitted to come into contact with the base plate. The PCB is connected to the measuring instrument, which in turn is connected to a measuring computer. The temperature sensors and the pressure sensor are connected to the computer via data lines. A controller uses a thermocouple to monitor the temperature of the measuring cell and uses heating cartridges to maintain it at a temperature of 70°C. The anode is supplied with 1.0 molar methanol solution via a peristaltic pump (Ismatech BV-GE). To supply the cathode, compressed air combined with mass flow meters (Brooks 5850S) are used. A maximum of two pumps and mass flow meters with various flow-through ranges can be automated simultaneously with the measuring computers. Before entering the cell the methanol solution is preheated to 70°C. The dissolved gases escaping during the process are separated with self-made gas separators.

3. Results and discussion

3.1. Neutron radiography combined with local current and temperature distribution measurements

For studies on the application scale the four different stack cells shown in Figure 1 were used. The flow field geometries A-ME15 (six-fold meander) and C-CH15 (channels) of cells no. 1 and 2 correspond to the geometries of the forklift stack. Cells no. 3 and 4 were fitted with the same anode flow fields (A-ME15), but a grid design instead of a channel design for the cathode flow fields (C-GR10). One side of each of the cathode flow fields of all four cells was either hydrophobized with 'Nano Holz&Stein' sealer (cells no. 1 and 3) or hydrophilized with 'KLINGERflon' spray (cells no. 2 and 4), so that for each flow field the surface properties of the channels were only changed in one half of the cell. In the radiographs and the current density and temperature distributions, in each case the treated halves appeared on the left and the untreated halves on the right. The measuring cells were loaded with average current densities 50, 150 or 250 mA/cm^2 and were supplied with air according to the λ values of 4 and 2 and for methanol according to a λ value of 4.

Figure 6 provides an overview of characteristic neutron radiographs of all four measuring cells, corresponding to an average current density of 150 mA/cm^2 and an air ratio of 4.

Place Figure 6 here

In the C-CH15 flow field, hydrophobic channel surfaces lead to a clearly different water distribution than untreated surfaces (see Figure 6, upper left figure). Figure 7 presents enlarged sections of different areas in the associated radiograph. The section immediately below the center of the image shows the

water distribution for hydrophobic and untreated cathode channels in comparison, see detail (a). In hydrophobic areas, in many channels droplets form whose width corresponds to the width of the channels. The ribs in the associated area are not prominent in the dry-normalized radiograph. In untreated channels, only much smaller droplets appear. Here, the ribs appear as dark vertical lines that indicate the uptake of water by the ribs. It should be noted that water penetration into the ribs was only observed if binder-free Sigraflex (expanded graphite) was used as flow field material and the surface of Sigraflex was not treated with hydrophobizing agent.

With this measuring cell including a multi-channel cathode flow field there is no unequivocal correlation between the surface properties of the channels and the current density distribution (a more detailed discussion is presented in section 3.2). Frequently, the current densities in the right half of the cell are higher than those of the left side. However, at the time of the radiograph presented here, the converse situation is the case.

Place Figure 7 here

Reasons for this may include accumulations of water at certain positions in the area of the untreated channels that are presented in the two remaining image sections (b) and (c). The section of the lower edge of the image presents the lowest anode channel and the area of the sealing frame. Directly at the lower edge there is water in the channels that impairs through-flow. The center section of the right half of the cell shows a nearly horizontal arrangement of water in adjacent channels. This arrangement is at the level of a horizontal adhesive strip that connects the ribs of the flow field with the back wall. Depending on the average current density and air flow, the existence of the

arrangement varies between invisible and extending across the full width of the right half of the cell.

In contrast to hydrophobic and untreated channels, in hydrophilic and untreated channels in the flow field C-CH15, no differences in the water distribution can be observed. This appears to be in contradiction to the similar contact angles of untreated and hydrophobic surfaces, see Table 2. However, the result can be explained in terms of water uptake, which is demonstrated in Figure 8, showing each of the sections directly below the center of the cell of cells 1 and 2:

Place Figure 8 here

The ribs take up water in the area of both the untreated and the hydrophilic channels. This means that under DMFC operating conditions the surface of the cathode channels and the side walls of the ribs, respectively, behave hydrophilic. In the channels, only small droplets evolve. In both halves of the cell, water occurs in the channels at the lower edge of the image, see Figure 7, detail (c). The current density distribution does not indicate any advantages of untreated or hydrophilic channels. Here too, water at the level of the adhesive strip can be observed for some operating points. The horizontal water arrangement again remains confined to the area of the untreated channels, associated with a lower average current density in the right half of the cell.

In the flow field C-GR10 of cell 3, at the investigated operating points larger accumulations of water form in the area of the hydrophobic surface, see Figure 6, bottom left image. In addition to the influence on the current density distribution, the water distribution also has an influence on the temperature distribution, which becomes especially evident in this cell. Figure 9 serves as an example for the current densities 50, 150 and 250 mA/cm^2 and an air ratio

of 4, showing characteristic neutron radiographs and the associated current density and temperature distributions.

Place Figure 9 here

At 50 mA/cm^2, negative segment current densities form in most of the left half of the cell (see green segments in the medium row of Figure 9). This is a well-known phenomenon observed at small current densities and air flow rates whenever the local air flow rate is so small – e.g. because it is blocked by water droplets in the flow field channels – that it falls below a critical value [8, 65, 66]. In this case, the so-called 'bi-functional regime' evolves: negative (electrolysis) currents occur in the air-starved region, whereas normal DMFC operation takes place in the well-supplied part of the cell. In one of our previous publications we already observed the bi-functional regime by measuring the local current distribution in small test cells [8]. It turned out that only in the case of untreated and hydrophobic cathode channels bi-functional operation appeared. We supposed that a local blocking of oxygen supply by water droplets was responsible for this phenomenon. Thanks to neutron radiography the blocking of cathode channels by water droplets can be demonstrated in the present work, see Figure 9. The blocking effect is mostly found in the left hydrophobized part of the cell. In the right part of the cell, fewer water droplets occur and no negative currents are observed. These results indicate a clear correlation between the water and current distributions unlike the measurements based on the channel cathode flow field design (see above). At higher current densities only one segment (light green) continues to show a strongly negative current caused by a measuring artifact. However, the partial blocking of cathode channels by water droplets in the left, hydrophobized part of the cathode flow field is still there. This has a direct impact on local performance: the average current density in the untreated right

side of the cell is always higher compared to that of the hydrophobized left part of the cell.

The temperature distribution shown in the bottom row of Figure 9 also reflects the different water distributions of the two halves of the cells. In the left half, the temperature in the upper part is elevated while in the right half, it is elevated in the lower part. For the current densities 150 and 250 mA/cm^2 the average temperature of the left half is higher than that of the right half. The temperature in the right half rises slightly from above to below. At the beginning of the measurements, the average temperatures of the two halves of the cells are balanced in each case. A possible explanation for the observed temperatures may be the special interaction between air flow and cell operation: The higher amount of water in the left half of the cell means that the air flow is more strongly impaired than in the right half, so that a larger share of the air volume flow supplies the right half. The low flow velocity in the left half enables elevated temperatures in the area, which roughly correlates with the area in which the usual exothermic fuel cell reaction takes place. In addition, in this area heat generation caused by the oxidation of permeated methanol can be expected. In the area below the endothermic reaction of the electrolytic operation takes place. The low flow velocity and the electrolytic operation suggest that in this area the oxygen concentration is barely sufficient for the oxidation of permeated methanol and, in turn, for heat generation. In the upper part of the right side of the cell the cooling influence of the air flow prevents a rise in temperature due to the lower air inlet temperature and an elevated uptake of gaseous water. Heat generation due to the proceeding reactions does not predominate until some distance from the air inlet. At the current densities 150 mA/cm^2 or 250 mA/cm^2 the air volume flow rate is three or five times higher, respectively, than for the current density 50 mA/cm^2 and the cooling effect of the air flow increases in the right half of the cell. The frequently observed temperature drop toward the outer sides and especially

toward the corners can be explained by the increased discharge of heat of the measuring cell at the outer surfaces.

As shown in the left half of the bottom left image of Figure 6, a hydrophilic surface improves the water discharge in the flow field C-GR10 compared to an untreated surface. While hardly any water is visible in the area of the hydrophilic surface, in the area of the untreated surface, depending on the operating point, various amounts of water can be observed. The relationship between the water volume and the air ratio is especially clear. With decreasing air ratio the level at which water evolves in the area of the untreated surface increases. A notable influence on the current density distribution cannot be identified for the operating points shown.

3.2 Spatially and temporally resolved measurements

By means of segmented cell technology, the locally and temporally dependent current was measured in dependence of the surface properties and the geometry of the cathode channels. Additionally, simultaneous measurements of the pressure drop along the cathode flow field channels and the overall performance were carried out (see Figures 10-12). In contrast to the neutron radiography experiments, these experiments were performed with stack cells where the *whole* cathode flow field area was either untreated, hydrophobized or hydrophilized. The results shown in the following were obtained at a temperature of 70°C, a current density of 150 mA/cm^2 and air ratios of 4 or 2. Three cathode flow field designs are compared: The channel C-CH15 design (Figure 10), the grid C-GR10 design (Figure 11) and the grid C-GR15 design (Figure 12). Figure 10 shows a decrease of the power density after one hundred (hydrophobic) or several hundred seconds (untreated/hydrophilic) of operation. As already shown in Ref. [67], the initial decrease of power density can be attributed to a temporary flooding of the cathode channels. This performance drop correlates quite well with a reverse change of the pressure

drop. There is also the rough correlation with the current distribution: The higher the power density, the lower is the range of segment currents and *vice versa*. In the course of the experiment the performance partially recovers which can be explained by a partial removal of water droplets. It is obvious from Figure 10 that the channel C-CH15 design causes substantial fluctuations of the overall power density, the local currents and the pressure drop, irrespective of the surface properties of the cathode channels. Although repeated experiments confirmed the principle effects it was hardly possible to reproduce the time curves after the power drop. Therefore, it is difficult to unravel the influence of the surface properties from the superimposed fluctuations caused by the channel C-CH15 design. It seems that the instability of operation obscures the differences of the C-CH15 flow fields.

Place Figure 10 here

The picture changes if a C-GR10 grid flow field is used (see Figure 11). There is no abrupt decrease in performance although the pressure drop increases significantly during the first minutes of the experiment. At the same time, the cell performance is about 10-20 % higher, the current distribution is more even and there is much less fluctuation in comparison to the results obtained with the C-CH15 channel flow field. The stability of operation is mainly due to the two-dimensional structure of the grid design, which allows air to by-pass local accumulations of water in the cathode channels. Because of the stable, defined and reproducible operational characteristics the influence of cathode flow field treatment becomes more evident. For instance, hydrophobic cathode channels have an unfavorable impact on the performance and homogeneity of the current distribution, see middle column in Figure 11. *Vice versa*, hydrophilic impregnation of the cathode channels enables not only a good performance and homogeneous current distribution, but in particular a low and temporally

stable pressure drop, see right column in Figure 11. The simple reason is that the hydrophilic surface of the channel walls prevents the formation of large water droplets that partially or completely block the channels, which would result in a large pressure drop.

However, even in the case of the hydrophilized channel surface the pressure drop of about 3 mbar is twice the value obtained with the C-CH15 channel flow field. This can be explained by the lower channel cross-section of the grid design C-GR10 (1 mm × 1 mm²) compared to the channel design C-CH15 (1.5 mm × 1.5 mm). High pressure drops are disadvantageous with respect to the overall efficiency of DMFC systems because a higher power of the air blower would be required. This drawback can be encountered by using the C-GR15 grid flow field with channel dimensions of 1.5 mm × 1.5 mm.

Place Figure 11 here

In Figure 12, the advantage of the C-GR15 cathode flow field design is demonstrated: In case of the hydrophilized sample (see right diagram below), the (stable!) pressure drop amounts to only 0.5 mbar, which is about 15 % or 30 % of the values obtained with C-GR10 and C-CH15, respectively. A comparison of Figure 11 and Figure 12 shows that for C-GR15 the irregularities in the current density distribution are more pronounced for hydrophobic channels than in the structure C-GR10 and the differences in the pressure difference curve are clearer. Hydrophilic channels exhibit the lowest and hydrophobic channels the highest increase in pressure difference after the start of the measurements. The more divergent operating behavior of the cells equipped with C-GR15 flow fields is mainly due to the higher channel cross section, leading to a decrease of air flow rate by a factor of 1.5 if the air ratio is

constant. The lower the air flow rate, the more prominent are differences caused by the surface treatment of flow fields.

Place Figure 12 here

Figure 13 shows the corresponding current density and temperature distributions. The similar current distribution of the three cells with differently pretreated flow fields is in line with the similar range of segment currents and time-dependent performance shown in the upper part of Figure 12. The temperature distribution for hydrophilic channels again suggests the most uniform air flow of all cases: In the upper two rows of segments (see bottom right picture of Figure 13), low and identical temperatures of 69.0°C are measured, which indicates the cooling effect of an unhindered air flow at the oxygen inlet and in the upper part of the cathode flow field. Furthermore, the average temperature amounts to 70.3°C, which is less than compared to the untreated cell (70.5°C) and the hydrophobized cell (71.1°C). Especially in the latter case high temperatures in the middle lower part of the cell suggest a severe blocking of air flow by water droplets in the channels (see bottom middle picture of Figure 13).

Place Figure 13 here

The full advantage of the hydrophilized C-GR15 flow field is realized at reduced air ratios, e.g. $\lambda_{air} = 2$ (see Figure 14, right diagrams): Compared to the results obtained with $\lambda_{air} = 4$ (Figure 12), the performance and homogeneity of the local current is hardly changed. This means that stable cell operation is possible even under low oxygen stoichiometries. Moreover, the

pressure drop decreases to a value as low as 0.2 mbar. The low difference in pressure with hydrophilic channels, whose fluctuations are not visible with the measurement resolution used, suggests continuous water transport.

Place Figure 14 here

Figure 15 shows the corresponding current density and temperature distributions. It can be seen that only the cell with hydrophobized cathode flow field (upper middle picture) shows a more uneven current distribution than at $\lambda_{air} = 4$. The low segment currents in the vicinity of the air outlet (bottom part) can be explained by a severe air starvation. This is not only caused by oxygen consumption (which applies also to the cells with untreated and hydrophilized flow fields) but is primarily due to local blocking of air flow by water droplets. The uneven air distribution is also evident from the inhomogeneous temperature distribution in the top row of segments close to the air inlet. For hydrophilic channels there are no signs of water accumulations. The comparison of the temperature distributions at $\lambda_{air} = 4$ (Figure 13) and $\lambda_{air} = 2$ (Figure 15) shows an elevated temperature level for the lower air stoichiometry. This is due to: (i) the lower cooling effect of a smaller air flow rate and (ii) less heat loss because of lower amount of water which has to be evaporated.

Place Figure 15 here

Conclusions

For the first time, the water distribution in the flow fields of large DMFC stack cells (314.75 cm²) was investigated by through-plane neutron radiography.

Measurements of current and temperature distributions were performed in combination with neutron radiography and time-dependent measurements of the overall performance and the pressure drop in the cathode flow field channels. The experiments reveal a superior performance of grid cathode flow fields compared to channel cathode flow fields. Grid flow fields provide a 10-20 % higher cell performance, a more even current distribution and much less fluctuations of cell operation. This advantage is due to the two-dimensional grid design, which allows air to by-pass local accumulations of water, making the cell less sensitive to the formation of water droplets. A more even and temporally stable local current does not only improve the performance, but may also be advantageous with respect to degradation. Locally high currents cause high overpotentials leading to a damage of local cell areas and in worst case, even cause degradation waves [68-70].

The full potential of the hydrophilized grid flow field is demonstrated at a reduced air ratio of 2 and a channel depth and width of each 1.5 mm. This combination allows high and stable performance with a pressure drop of only 0.2 mbar. For DMFC system operation, this has decisive advantages: the hydrophilized C-GR15 flow field allows stable operating conditions even at low air flows, enabling a reduction of the blower power, which increases the overall system efficiency. Additionally, lower air flow rates enable higher operating temperatures in self-heating stacks, leading to higher efficiencies, too.

Acknowledgements

We are obliged to Gerald Zehl from HZB Berlin for performing the contact angle measurements. Funding of the project RuN-PEM (grant number: 03SF0324) by the Federal Ministry of Education and Research (BMBF) is gratefully acknowledged.

References

[1] Liu X, Guo H, Ma C. Water flooding and two-phase flow in cathode channels of proton exchange membrane fuel cells. *Journal of Power Sources* 2006; **156**(2):267–280. DOI: 10.1016/j.jpowsour.2005.06.027

[2] Weng F-B, Su A, Hsu C-Y. The study of the effect of gas stoichiometric flow rate on the channel flooding and performance in a transparent fuel cell. *International Journal of Hydrogen Energy* 2007; **32**(6):666–676. DOI: 10.1016/j.ijhydene.2006.06.066

[3] Park Y-C, Peck D-H, Dong S-K, Kim S-K, Lim S, Jung D-H, et al. Operating characteristics and performance stability of 5 W class direct methanol fuel cell stacks with different cathode flow patterns. *International Journal of Hydrogen Energy* 2011; **36**(2):1853–1861. DOI: 10.1016/j.ijhydene.2010.02.018

[4] Barbir F, Gorgun H, Wang X. Relationship between pressure drop and cell resistance as a diagnostic tool for PEM fuel cells. *Journal of Power Sources* 2005; **141**(1):96–101. DOI: 10.1016/j.jpowsour.2004.08.055

[5] Anderson R, Zhang L, Ding Y, Blanco M, Bi X, Wilkinson DP. A critical review of two-phase flow in gas flow channels of proton exchange membrane fuel cells. *Journal of Power Sources* 2010; **195**(15):4531–4553. DOI: 10.1016/j.jpowsour.2009.12.123

[6] Liu X, Guo H, Ye F, Ma CF. Flow dynamic characteristics in flow field of proton exchange membrane fuel cells. *International Journal of Hydrogen Energy* 2008; **33**(3):1040–1051. DOI: 10.1016/j.ijhydene.2007.11.018

[7] Schröder A, Wippermann K, Mergel J, Lehnert W, Stolten D, Sanders T, et al. Combined local current distribution measurements and high resolution neutron radiography of operating Direct Methanol Fuel Cells. *Electrochemistry Communications* 2009; **11**(8):1606-1609.

[8] Schröder A, Wippermann K, Zehl G, Stolten D. The influence of cathode flow field surface properties on the local and time-dependent performance of direct methanol fuel cells. *Electrochemistry Communications* 2010; **12**(10):1318-1321. 10.1016/j.elecom.2010.07.009

[9] Hartnig C, Manke I, Schloesser J, Krüger P, Kuhn R, Riesemeier H, et al. High resolution synchrotron X-ray investigation of carbon dioxide evolution in operating direct methanol fuel cells. *Electrochemistry Communications* 2009; **11**(8):1559-1562.

[10] Seemann R, Brinkmann M, Kramer EJ, Lange FF, Lipowsky R. Wetting morphologies at microstructured surfaces. *Proceedings of the National Academy of Sciences of the United States of America* 2005; **102**(6):1848–1852. 10.1073/pnas.0407721102

[11] Chen Y, Melvin LS, Rodriguez S, Bell D, Weislogel MM. Capillary driven flow in micro scale surface structures. *Microelectronic Engineering* 2009; **86**(4–6):1317–1320. DOI: 10.1016/j.mee.2009.02.016

[12] Extrand CW. Relation between Contact Angle and the Cross-Sectional Area of Small, Sessile Liquid Drops. *Langmuir* 2006; **22**8431–8434.

[13] Kumbur EC, Sharp KV, Mench MM. Liquid droplet behavior and instability in a polymer electrolyte fuel cell flow channel. *Journal of Power Sources* 2006; **161**(1):333–345. DOI: 10.1016/j.jpowsour.2006.04.093

[14] Owejan JP, Trabold TA, Jacobson DL, Arif M, Kandlikar SG. Effects of flow field and diffusion layer properties on water accumulation in a PEM fuel cell. *International Journal of Hydrogen Energy* 2007; **32**(17):4489–4502. DOI: 10.1016/j.ijhydene.2007.05.044

[15] Bazylak A, Heinrich J, Djilali N, Sinton D. Liquid water transport between graphite paper and a solid surface. *Journal of Power Sources* 2008; **185**(2):1147–1153. DOI: 10.1016/j.jpowsour.2008.07.031

[16] Turhan A, Kim S, Hatzell M, Mench MM. Impact of channel wall hydrophobicity on through-plane water distribution and flooding behavior in a polymer electrolyte fuel cell. *Electrochimica Acta* 2010; **55**(8):2734-2745. 10.1016/j.electacta.2009.11.095

[17] Chaudhury MK, Whitesides GM. How to make water run uphill. *Science* 1992; **256**(5063):1539–1544.

[18] Trabold TA, Owejan JP, Gagliardo JJ, Jacobson DL, Hussey DS, Arif M. Use of neutron imaging for proton exchange membrane fluel cell (PEMFC) performance analysis and design. In: Vielstich W, Yokokawa H, Gasteiger HA, editors. Handbook of fuel cells: Fundamentals, Technology and Applications. New York: Wiley; 2009. p. 658–672.

[19] Manke I, Markötter H, Tötzke C, Kardjilov N, Grothausmann R, Dawson M, et al. Investigation of Energy-Relevant Materials with Synchrotron X-Rays and Neutrons. *Adv Eng Mater* 2011; **13**(8):712-729. 10.1002/adem.201000284

[20] N. Kardjilov, I. Manke, A. Hilger, M. Strobl, Banhart J. Neutron imaging in materials science. *Materials Today* 2011; **14**(6):248-256.

[21] Banhart J, Borbely A, Dzieciol K, Garcia-Moreno F, Manke I, Kardjilov N, et al. X-ray and neutron imaging - Complementary techniques for materials science and engineering. *International Journal of Materials Research* 2010; **101**(9):1069-1079.

[22] Lehmann E. Recent improvements in the methodology of neutron imaging. *Pramana Journal of Physics* 2008; **71**(4):653-661.

[23] Strobl M, Manke I, Kardjilov N, Hilger A, Dawson M, Banhart J. Advances in neutron radiography and tomography. *Journal of Physics D-Applied Physics* 2009; **42**(24):243001. DOI: 10.1088/0022-3727/42/24/243001

[24] Owejan JP, Trabold TA, Jacobson DL, Baker DR, Hussey DS, Arif M. In situ investigation of water transport in an operating PEM fuel cell using neutron radiography: Part 2 - Transient water accumulation in an interdigitated cathode flow field. *International Journal of Heat and Mass Transfer* 2006; **49**(25-26):4721-4731.

[25] Kramer D, Zhang J, Shimoi R, Lehmann E, Wokaun A, Shinohara K, et al. In situ diagnostic of two-phase flow phenomena in polymer electrolyte fuel cells by neutron imaging: Part A. Experimental, data treatment, and quantification. *Electrochimica Acta* 2005; **50**(13):2603-2614.

[26] Hartnig C, Manke I, Kardjilov N, Hilger A, Grünerbel M, Kaczerowski J, et al. Combined neutron radiography and locally resolved current density measurements of operating PEM fuel cells. *Journal of Power Sources* 2008; **176**(2):452-459.

[27] Bellows RJ, Lin MY, Arif M, Thompson AK, Jacobson D. Neutron Imaging Technique for In Situ Measurement of Water Transport Gradients within Nafion in Polymer Electrolyte Fuel Cells. *Journal of The Electrochemical Society* 1999; **146**(3):1099 - 1103.

[28] Boillat P, Frei G, Lehmann EH, Scherer GG, Wokaun A. Neutron Imaging Resolution Improvements Optimized for Fuel Cell Applications. *Electrochemical and Solid-State Letters* 2010; **13**(3):B25-B27.

[29] Maier W, Arlt T, Wannek C, Manke I, Riesemeier H, Krüger P, et al. In-situ synchrotron x-ray radiography on high temperature polymer electrolyte fuel cells. *Electrochemistry Communications* 2010; **12**(10):1436-1438.

[30] Hickner MA, Siegel NP, Chen KS, Hussey DS, Jacobson DL, Arif M. Understanding Liquid Water Distribution and Removal Phenomena in an Operating PEMFC via Neutron Radiography. *Journal of The Electrochemical Society* 2008; **155**(3):B294–B302. 10.1149/1.2825298

[31] Kuhn R, Scholta J, Krüger P, Hartnig C, Lehnert W, Arlt T, et al. Measuring Device for Synchrotron X-ray Imaging and First Investigation of High Temperature PEM Fuel Cells. *Journal of Power Sources* 2010. doi:10.1016/j.jpowsour.2010.11.025

[32] Chen Y-S, Peng H, Hussey DS, Jacobson DL, Tran DT, Abdel-Baset T, et al. Water distribution measurement for a PEMFC through neutron radiography. *Journal of Power Sources* 2007; **170**(2):376-386. 10.1016/j.jpowsour.2007.03.076

[33] Fu RS, Pasaogullari U, Hussey DS, Jacobson DL, Arif M. Neutron radiography imaging of simulated non-isothermal start-up of a polymer electrolyte fuel cell. *ECS Transactions* 2007; **11**(1):395–401.

[34] Gagliardo JJ, Owejan JP, Trabold TA, Tighe TW. Neutron radiography characterization of an operating proton exchange membrane fuel cell with localized current distribution measurements. *Nuclear Instruments and Methods in Physics Research Section A: Accelerators, Spectrometers, Detectors and Associated Equipment* 2009; **605**(1–2):115-118. 10.1016/j.nima.2009.01.145

[35] Hussey DS, Jacobson DL, Arif M, Owejan JP, Gagliardo JJ, Trabold TA. Neutron images of the through-plane water distribution of an operating PEM fuel cell. *Journal of Power Sources* 2007; **172**(1):225–228. DOI: 10.1016/j.jpowsour.2007.07.036

[36] Manke I, Hartnig C, Kardjilov N, Messerschmidt M, Hilger A, Strobl M, et al. Characterization of water exchange and two-phase flow in porous gas diffusion

materials by hydrogen-deuterium contrast neutron radiography. *Applied Physics Letters* 2008; **92**244101. 10.1063/1.2946664

[37] Owejan JP, Trabold TA, Gagliardo JJ, Jacobson DL, Carter RN, Hussey DS, et al. Voltage instability in a simulated fuel cell stack correlated to cathode water accumulation. *Journal of Power Sources* 2007; **171**(2):626–633. DOI: 10.1016/j.jpowsour.2007.06.174

[38] Park J, Li X, Tran D, Abdel-Baset T, Hussey DS, Jacobson DL, et al. Neutron imaging investigation of liquid water distribution in and the performance of a PEM fuel cell. *International Journal of Hydrogen Energy* 2008; **33**(13):3373–3384. DOI: 10.1016/j.ijhydene.2008.03.019

[39] Schneider IA, Kramer D, Wokaun A, Scherer GG. Spatially resolved characterization of PEFCs using simultaneously neutron radiography and locally resolved impedance spectroscopy. *Electrochemistry Communications* 2005; **7**(12):1393-1397. 10.1016/j.elecom.2005.09.017

[40] Spernjak D, Advani SG, Prasad AK. Simultaneous Neutron and Optical Imaging in PEM Fuel Cells. *Journal of The Electrochemical Society* 2009; **156**(1):B109–B117. 10.1149/1.3009585

[41] Spernjak D, Prasad AK, Advani SG. In situ comparison of water content and dynamics in parallel, single-serpentine, and interdigitated flow fields of polymer electrolyte membrane fuel cells. *Journal of Power Sources* 2010; **195**(11):3553–3568. DOI: 10.1016/j.jpowsour.2009.12.031

[42] Turhan A, Heller K, Brenizer JS, Mench MM. Quantification of liquid water accumulation and distribution in a polymer electrolyte fuel cell using neutron imaging. *Journal of Power Sources* 2006; **160**(2):1195-1203.

[43] Yoshizawa K, Ikezoe K, Tasaki Y, Kramer D, Lehmann EH, Scherer GG. Analysis of Gas Diffusion Layer and Flow-Field Design in a PEMFC Using Neutron Radiography. *Journal of The Electrochemical Society* 2008; **155**(3):B223–B227. 10.1149/1.2823003

[44] Lehnert W. Porous media. Polymer Electrolyte Fuel Cells Introduction Course. WBZU UlmSeptember 2010.

[45] Zhang J, Kramer D, Shimoi R, Ono Y, Lehmann E, Wokaun A, et al. In situ diagnostic of two-phase flow phenomena in polymer electrolyte fuel cells by neutron imaging: Part B. Material variations. *Electrochimica Acta* 2006; **51**(13):2715-2727.

[46] Manke I, Hartnig C, Kardjilov N, Riesemeier H, Goebbels J, Kuhn R, et al. In situ Synchrotron X-ray Radiography Investigations of Water Transport in PEM Fuel Cells. *Fuel Cells* 2010; **10**(1):26-34.

[47] Markötter H, Manke I, Krüger P, Arlt T, Haussmann J, Klages M, et al. Investigation of 3D water transport paths in gas diffusion layers by combined in-situ synchrotron X-ray radiography and tomography. *Electrochemistry Communications* 2011; **13**(9):1001-1004. 10.1016/j.elecom.2011.06.023

[48] Geiger AB, Tsukada A, Lehmann E, Vontobel P, Wokaun A, Scherer GG. In situ investigation of two-phase flow patterns in flow fields of PEFC's using neutron radiography. *Fuel Cells* 2003; **2**92–98.

[49] Lehmann EH, Vontobel P, Kardjilov N. Hydrogen distribution measurements by neutrons. *Applied Radiation and Isotopes* 2004; **61**(4):503–509. DOI: 10.1016/j.apradiso.2004.03.075

[50] Kramer D, Lehmann E, Frei G, Vontobel P, Wokaun A, Scherer GG. An on-line study of fuel cell behavior by thermal neutrons. *Nuclear Instruments and Methods in Physics Research Section A: Accelerators, Spectrometers, Detectors and Associated Equipment* 2005; **542**(1–3):52-60. 10.1016/j.nima.2005.01.011

[51] Janßen H, Blum L, Kimiaie N, Maintz A, Mergel J, Müller M, et al. Performance Characterization of a 4-Wheel DMFC Scooter. *Proceedings 3rd European PEFC Forum, 04-08072005, Lucerne, Switzerland*.

[52] Nölke M. Entwicklung, Auslegung und Umsetzung eines DMFC-Systems der kW-Klasse *Schriften des Forschungszentrums Jülich Reihe Energietechnik/Energy Technology 64, Forschungszentrum Jülich, 2007, ISBN: 3-89336-481-1, ISSN: 1433-5522, http://hdlhandlenet/2128/2600*.

[53] http://www.sglgroup.com/export/sites/sglcarbon/_common/downloads/products/product-groups/nm/Mobility/DS_SIGRACET_BBP4_EU_e.pdf, call date: 12.01.2012

[54] http://www.sglgroup.com/cms/international/products/product-groups/eg/automotive-and-industrial-gaskets-made-of-flexible-graphite/downloads.html?__locale=en, call date: 12.01.2012.

[55] Kardjilov N, Hilger A, Manke I, Strobl M, Dawson M, Williams S, et al. Neutron tomography instrument CONRAD at HZB. *Nuclear Instruments and Methods in Physics Research Section A: Accelerators, Spectrometers, Detectors and Associated Equipment* 2011; **651**(1):47-52. 10.1016/j.nima.2011.01.067

[56] Kardjilov N, Hilger A, Manke I, Strobl M, Dawson M, Banhart J. New trends in neutron imaging. *Nuclear Instruments and Methods in Physics Research Section A: Accelerators, Spectrometers, Detectors and Associated Equipment* 2009; **605**(1-2):13-15.

[57] Kardjilov N, Dawson M, Hilger A, Manke I, Strobl M, Penumadu D, et al. A highly adaptive detector system for high resolution neutron imaging. *Nuclear Instruments and Methods in Physics Research Section A: Accelerators, Spectrometers, Detectors and Associated Equipment* 2011; DOI:10.1016/j.nima.2011.01.067.

[58] Ch. Tötzke, Manke I, Arlt T, Markötter H, Kardjilov N, Hilger A, et al. High resolution large area neutron imaging detector for fuel cell research. *Journal of Power Sources* 2011; **196**(10):4631-4637.

[59] http://www.oca.eu/guillot/ASTEP/docs/Andor%20Technology%20-%20iKon%20DW436.pdf, call date: 12.01.2012.

[60] Tötzke C, Manke I, Arlt T, Markötter H, Kardjilov N, Hilger A, et al. Investigation of fuel cells using scanning neutron imaging and a focusing neutron guide. *Nuclear Instruments and Methods in Physics Research Section A: Accelerators, Spectrometers, Detectors and Associated Equipment* 2012; **663**(1):48-54. 10.1016/j.nima.2011.09.054

[61] Kardjilov N, Hilger A, Dawson M, Manke I, Banhart J, Strobl M, et al. Neutron tomography using an elliptic focusing guide. *Journal of Applied Physics* 2010; **108**(034905):1–4. 10.1063/1.3467796

[62] Baumhöfer T. Ortsaufgelöste Messung und Modellierung von Impedanzspektren an Brennstoffzellen [Diplomarbeit]. Aachen: RWTH Aachen; 2008.

[63] Maxim Integrated Products: Datenblatt DS18B20, http://datasheets.maximic.com/en/ds/DS18B20.pdf, call date: 17.11.2010.

[64] Freescale Semiconductor: Integrated Silicon Pressure Sensor, http://www.freescale.com/files/sensors/doc/data_sheet/MPX5010.pdf, call date: 17.11.2010.

[65] Kulikovsky AA, Schmitz H, Wippermann K, Mergel J, Fricke B, Sanders T, et al. DMFC: Galvanic or electrolytic cell? *Electrochemistry Communications* 2006; **8**(5):754–760. DOI: 10.1016/j.elecom.2006.03.011

[66] Kulikovsky AA, Schmitz H, Wippermann K, Mergel J, Fricke B, Sanders T, et al. Bifunctional activation of a direct methanol fuel cell. *Journal of Power Sources* 2007; **173**(1):420-423. 10.1016/j.jpowsour.2007.04.072

[67] Schröder A, Wippermann K, Lehnert W, Stolten D, Sanders T, Baumhöfer T, et al. The influence of gas diffusion layer wettability on direct methanol fuel cell performance: A combined local current distribution and high resolution neutron radiography study. *Journal of Power Sources* 2010; **195**(15):4765-4771.

[68] Kulikovsky AA, Scharmann H, Wippermann K. Dynamics of fuel cell performance degradation. *Electrochemistry Communications* 2004; **6**(1):75-82. 10.1016/j.elecom.2003.10.018

[69] Kulikovsky AA, Electrostatic broadening of current-free spots in a fuel cell stack: The mechanism of stack aging? *Electrochemistry Communications* 2006; **8**(8):1225-1228. 10.1016/j.elecom.2006.05.010

[70] Kulikovsky AA, Chapter 4 - Quasi-2D model of a fuel cell. Analytical Modelling of Fuel Cells. Amsterdam: Elsevier; 2010. p. 117-192.

Figure captions:

Figure 1: Design of the flow fields for stack cell measurements in the through-plane viewing direction: anode flow field with six-fold meander ('A-ME15', upper left); cathode flow fields with channel structure (width = depth = 1.5 mm, see 'C-CH15' / upper right) or grid structure (edge length/distance between the cubes = 1.0 mm, see 'C-GR10' / lower left, edge length/distance of the cubes = 1.5 mm, see 'C-GR15' / lower right).

Figure 2: Printed circuit board for the cell design in through-plane viewing direction.

Figure 3: Exploded view of the cell design in the through-plane viewing direction.

Figure 4: Sketch of the neutron source, neutron guide and the camera set-up. Not to scale, especially the curvature is exaggerated.

Figure 5: Beam characteristics with widened neutron radiation showing various brightnesses. Left: contrast was set to the whole radiograph, right: contrast was set to the maximum intensity in the middle of the radiograph. Differing illuminations lead to differing signal-to-noise-ratios.

Figure 6: Cells no.1-4: Influence of the surface properties and design of cathode flow field; in each case, left side of the cathode channels treated; UNT: untreated, HPO: treated with hydrophobizing agent, HPI: treated with hydrophilizing agent; C-CH15: Cathode flow field with 1.5 mm channels (width / height), C-GR10: Cathode flow field with 1.0 mm × 1.0 mm × 1.0 mm cubes; j = 150 mA/cm^2, $\lambda_{MeOH} = 4$, $\lambda_{air} = 4$, T = 70°C.

Figure 7: Complete radiograph and enlarged sections of cell no.1 taken from Figure 6; detail (a): comparison of hydrophobic and untreated flow field areas near the center of cell no.1; detail (b): region of untreated flow field area above the horizontal adhesive strip; detail (c) region of lowest anode channel and

area of sealing frame; dry normalized; j = 150 mA/cm^2, λ_{MeOH} = 4, λ_{air} = 4, T = 70°C.

Figure 8: Detailed pictures of the center of cells no.1 (a) and no.2 (b) taken from the middle area of Figure 6; in each case, the left side of the cathode channels is treated; UNT: untreated, HPO: treated with hydrophobizing agent, HPI: treated with hydrophilizing agent; dry normalized, j = 150 mA/cm^2, λ_{MeOH} = 4, λ_{air} = 4, T = 70°C.

Figure 9: Influence of current density and hydrophobic surface properties in the flow field C-GR10, example of cell no.3; top row: Neutron radiographs showing the water distribution; medium row: current distribution; bottom row: temperature distribution; in each case, the cathode channels on the right side of the flow field were untreated (UNT), whereas those on the left side were treated with hydrophobizing agent (HPO); dry normalized, λ_{MeOH} = 4, λ_{air} = 4, T = 70 °C.

Figure 10: Operating behavior of the flow field C-CH15 as a function of surface properties; treatment of the cathode channels: UNT; untreated, HPO: treated with hydrophobizing agent, HPI: treated with hydrophilizing agent; j = 150 mA/cm^2, λ_{MeOH} = 4, λ_{air} = 4, T = 70°C.

Figure 11: Operating behavior of the flow field C-Gr10 as a function of surface properties at an air ratio of 4; treatment of the cathode channels: UNT; untreated, HPO: treated with hydrophobizing agent, HPI: treated with hydrophilizing agent; j = 150 mA/cm^2, λ_{MeOH} = 4, T = 70°C.

Figure 12: Operating behavior of the flow field C-Gr15 as a function of surface properties at an air ratio of 4; treatment of the cathode channels: UNT; untreated, HPO: treated with hydrophobizing agent, HPI: treated with hydrophilizing agent; j = 150 mA/cm^2, λ_{MeOH} = 4, T = 70°C.

Figure 13: Current density (top) and temperature distribution (bottom) of the flow field C-Gr15 as a function of surface properties at an air ratio of 4;

treatment of the cathode channels: UNT; untreated, HPO: treated with hydrophobizing agent, HPI: treated with hydrophilizing agent; j = 150 mA/cm^2, λ_{MeOH} = 4, T = 70°C.

Figure 14: Operating behavior of the flow field C-Gr15 as a function of surface properties at an air ratio of 2; treatment of the cathode channels: UNT; untreated, HPO: treated with hydrophobizing agent, HPI: treated with hydrophilizing agent; j = 150 mA/cm^2, λ_{MeOH} = 4, T = 70°C.

Figure 15: Current density (top) and temperature distribution (bottom) of the flow field C-Gr15 as a function of surface properties at an air ratio of 2; treatment of the cathode channels: UNT; untreated, HPO: treated with hydrophobizing agent, HPI: treated with hydrophilizing agent; j = 150 mA/cm^2, λ_{MeOH} = 4, T = 70°C.

Table captions:

Table 1: Flow field designs and dimensions

Table 2: Resulting contact angles of the materials used for flow field fabrication in consequence of the surface preparations. UNT: untreated surface, HPO: surface hydrophobized by treatment with 'Nano Holz&Stein' sealant of Oberflächentechnik Preimeß GmbH, HPI: surface hydrophilized by treatment with 'KLINGERflon-Spray' of Klinger GmbH.

Figures:

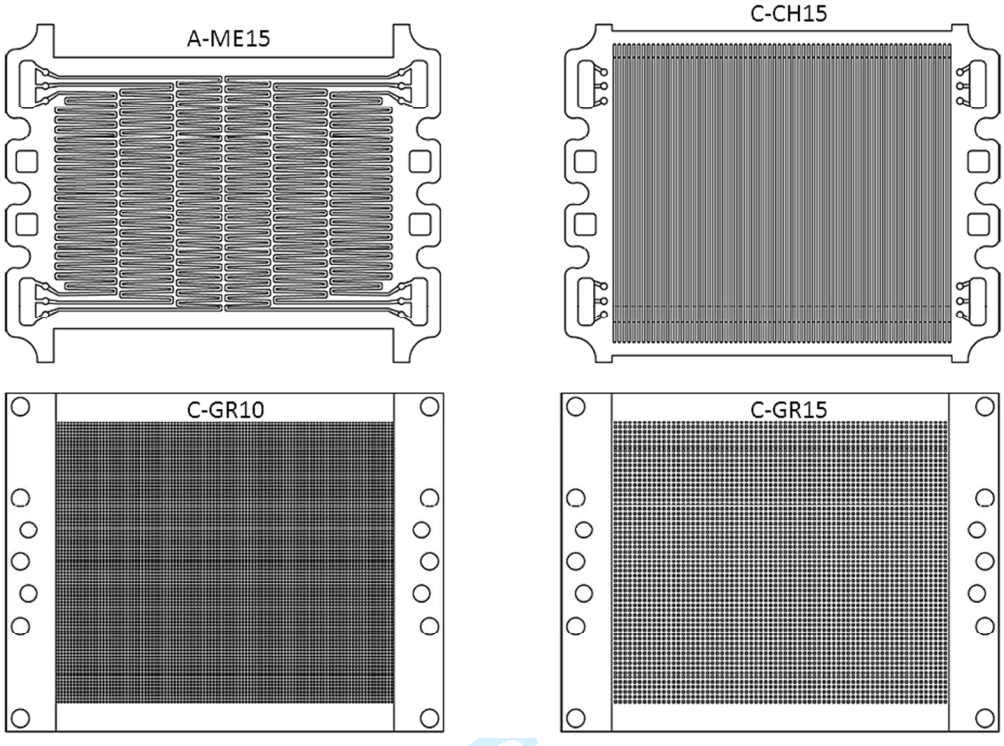

Figure 1

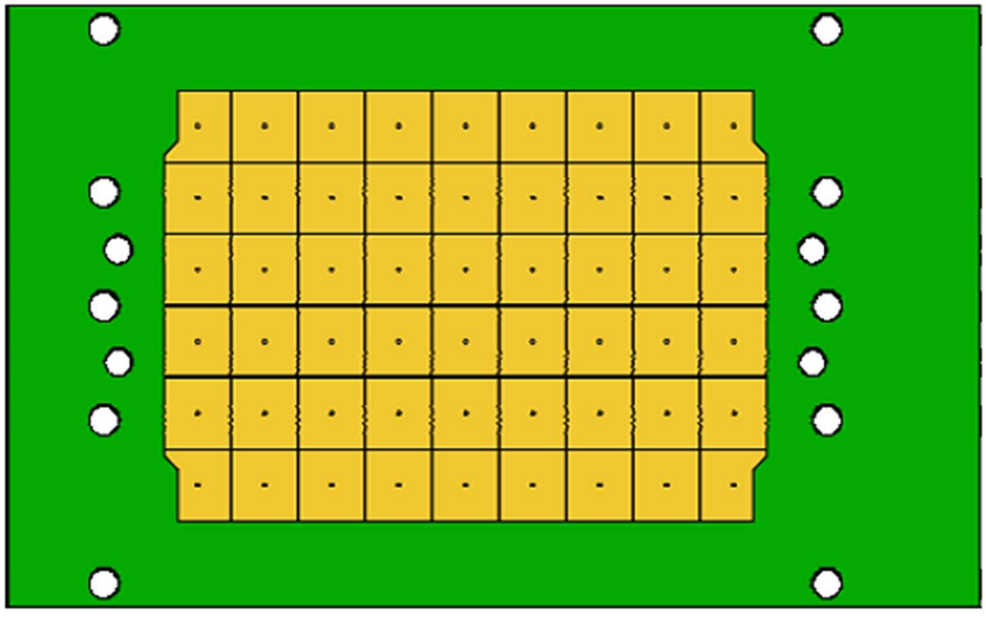

Figure 2

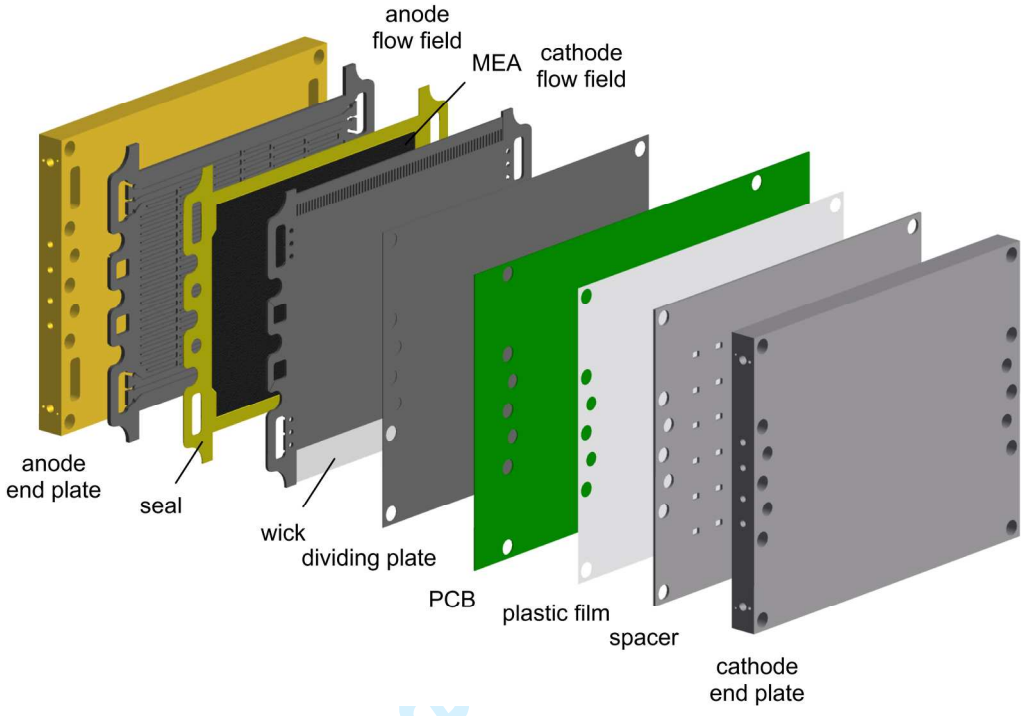

Figure 3

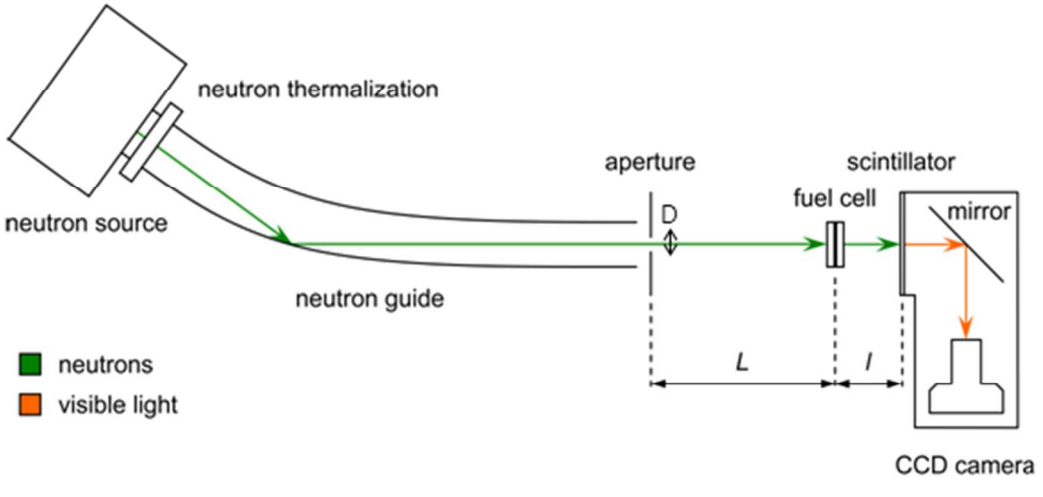

Figure 4

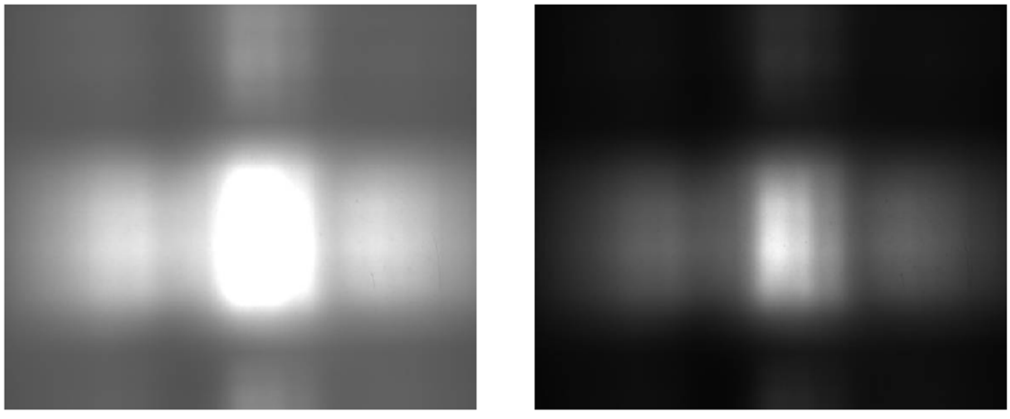

Figure 5

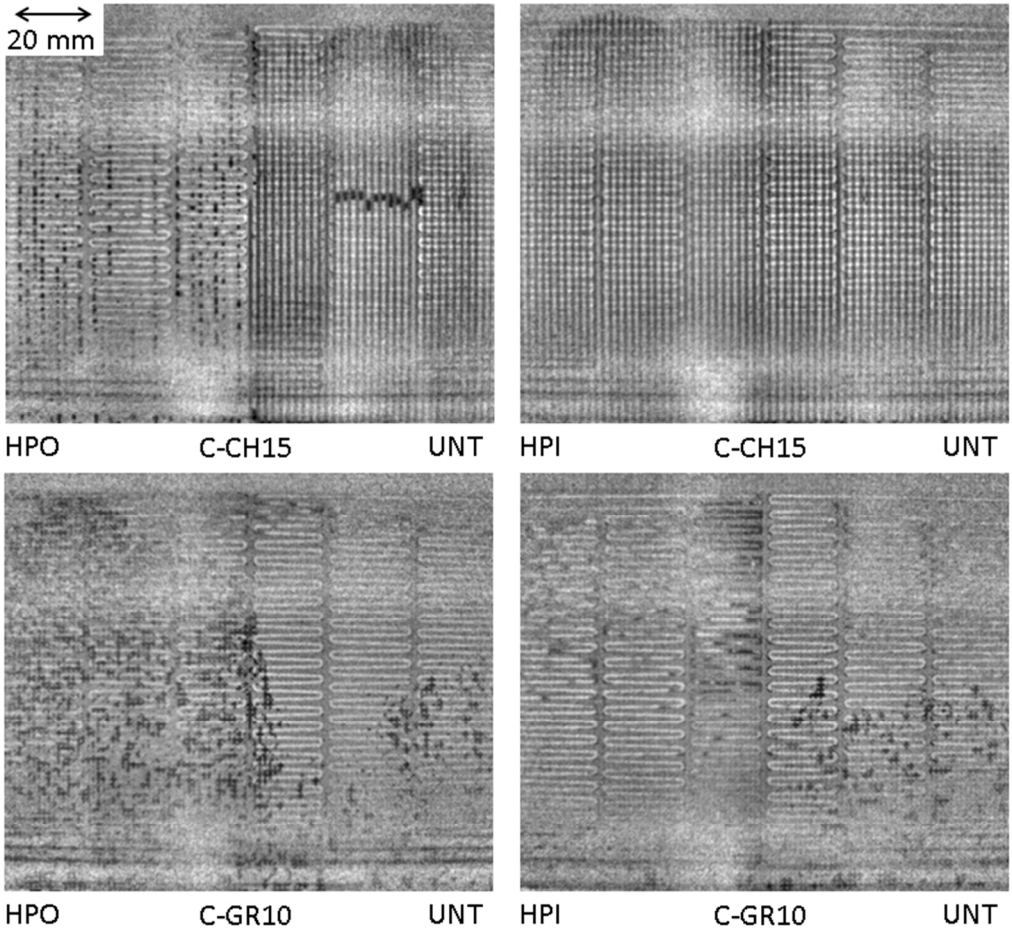

Figure 6

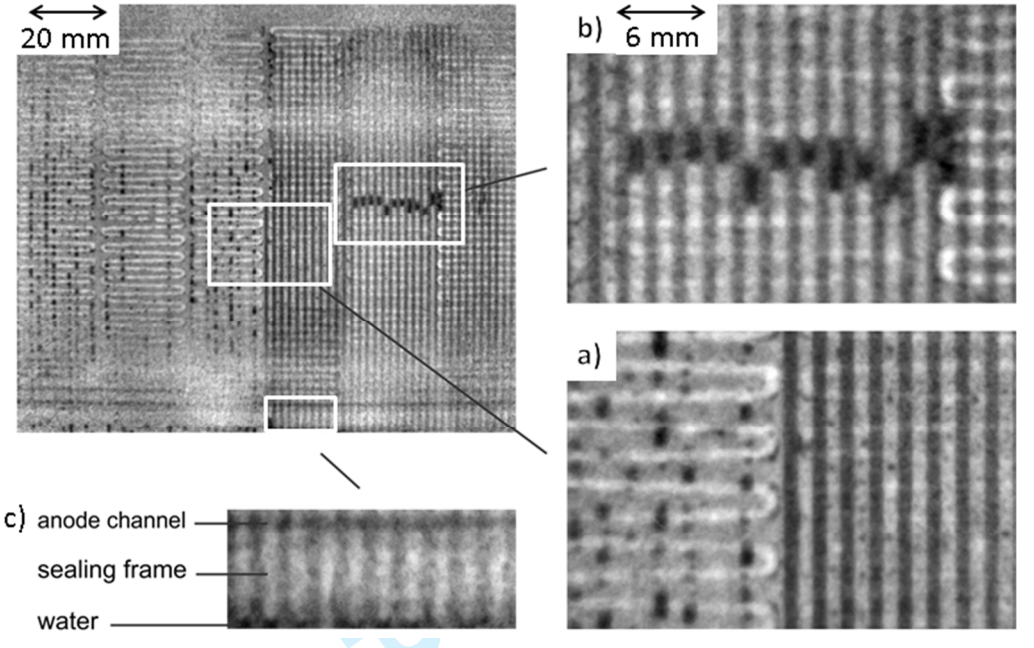

Figure 7

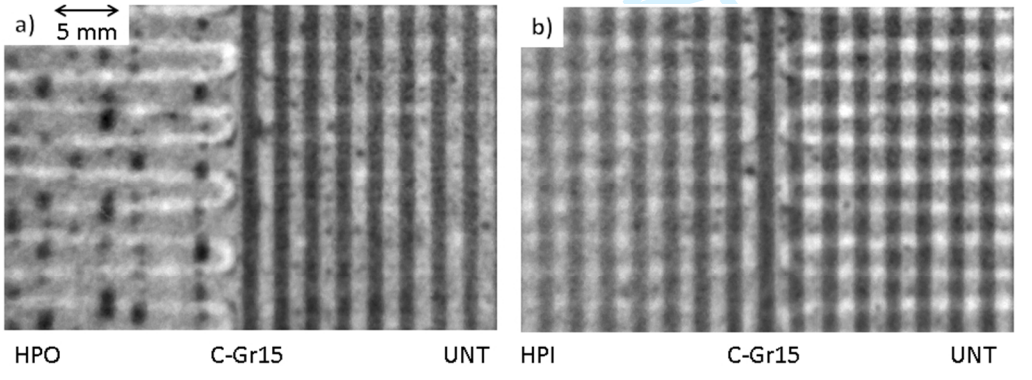

Figure 8

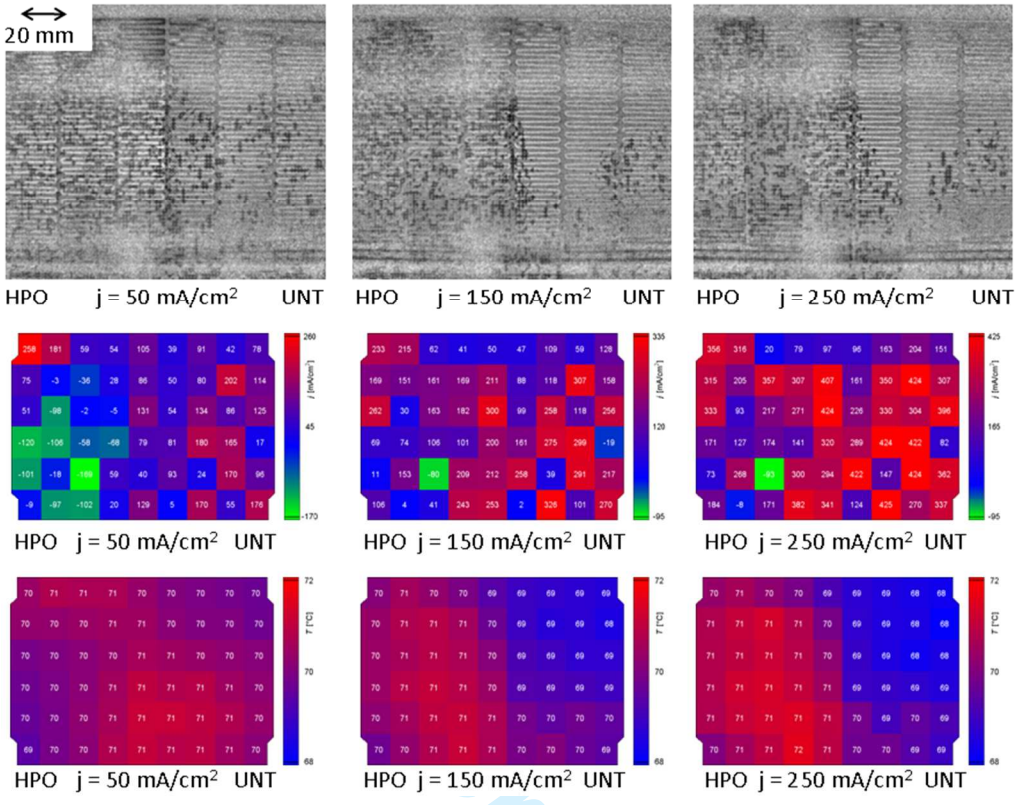

Figure 9

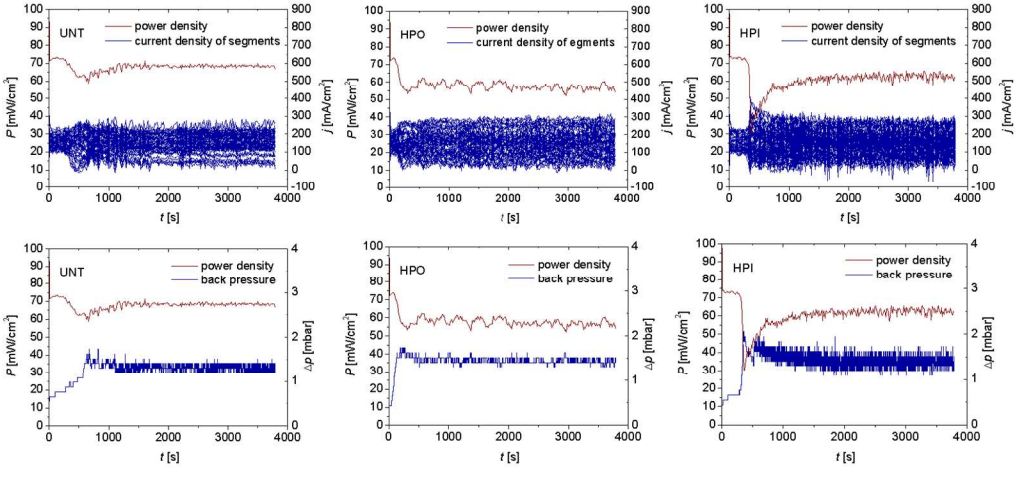

Figure 10

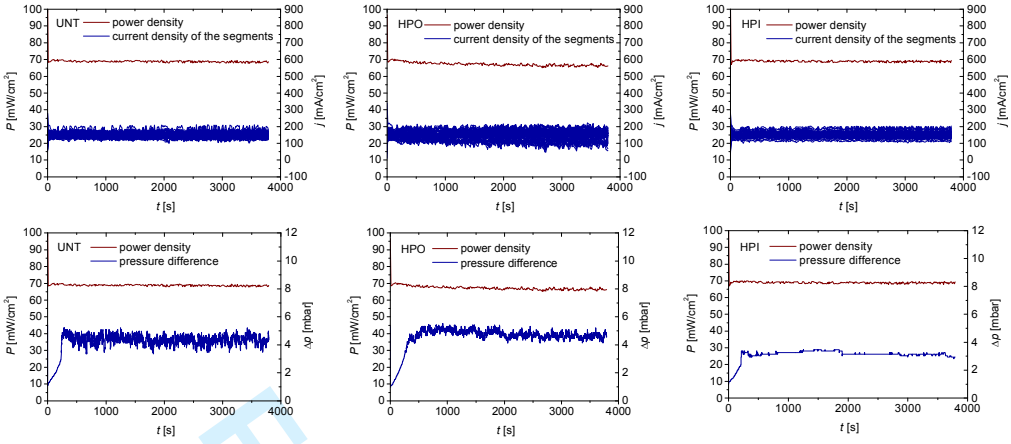

Figure 11

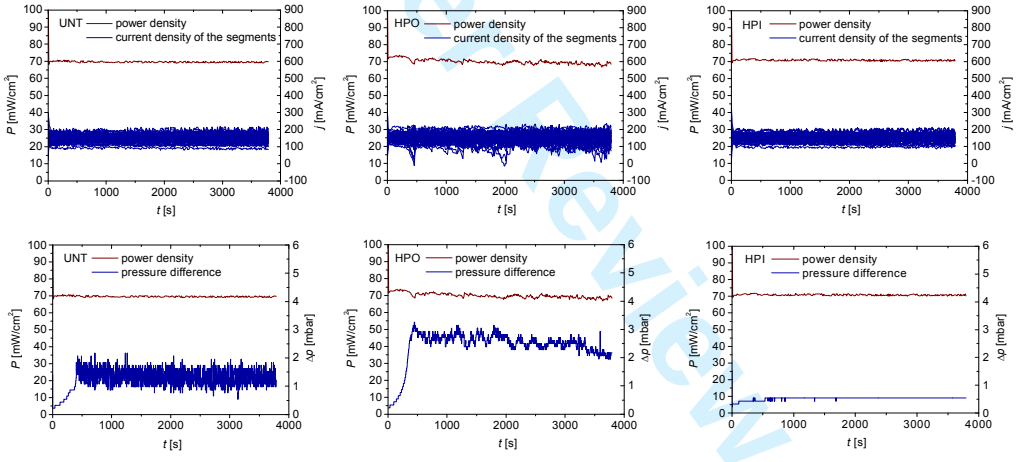

Figure 12

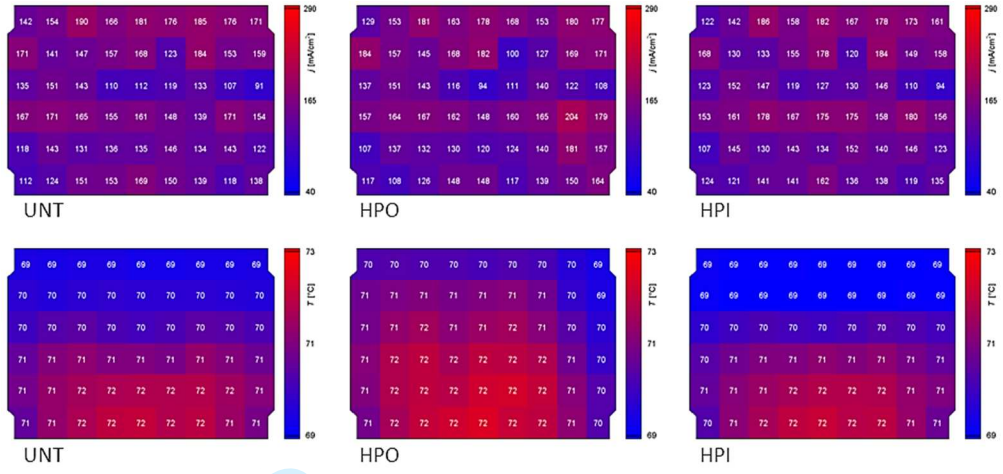

Figure 13

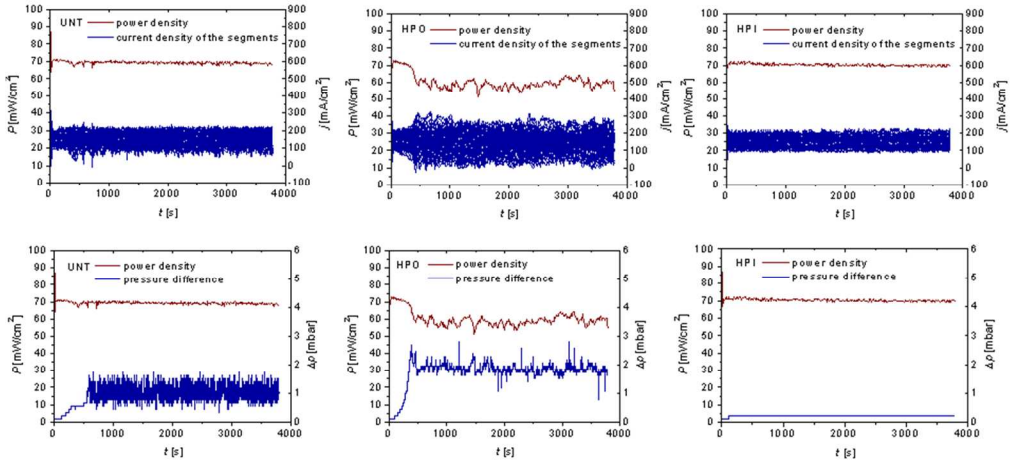

Figure 14

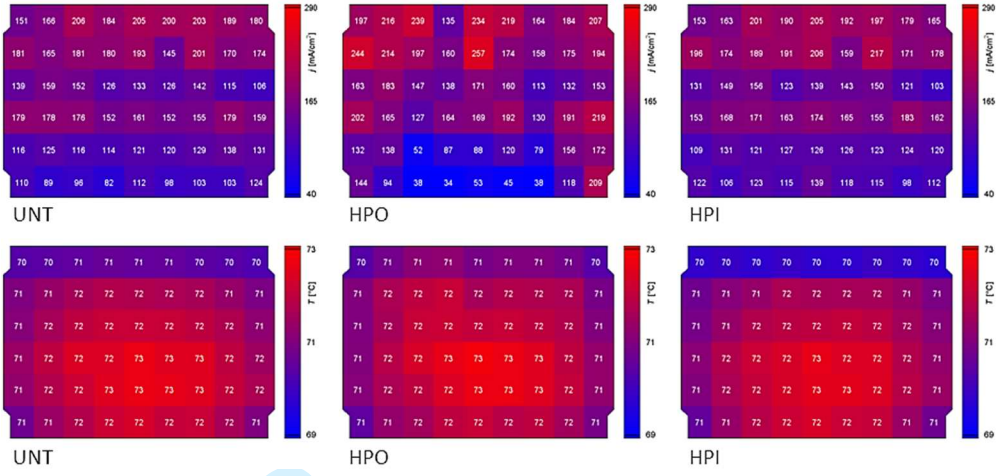

Figure 15

Tables:

flow field design A = anode C = cathode	method / -	electrode surface / cm^2	land width / mm	channel width / mm	channel height / mm	channel length / mm	sum of channel cross sections / mm^2	area ratio of channel to land / %	flow rate / mm s^{-1}
A-ME15, 6-fold meander	SCT[1]/ NR[2]	314.75	1.0-2.3	1.5	1.5	1523-1596	13.5	44.6	24.16
C-CH15, channel	SCT[1]/ NR[2]	314.75	1.5	1.5	1.5	151	157.5	49.9	368
C-GR10, grid	SCT[1]/ NR[2]	314.75	1.0	1.0	1.0	151	105.0-209.0[3]	74.4	277-552
C-GR15, grid	SCT[1]	314.75	1.5	1.5	1.5	151	157.5-312.75[3]	74.3	185-368

[1] SCR = segmented cell technology, [2] NR = neutron radiography; [3]lower value: grid design, higher value: channel design

Table 1

material	UNT	HPO	HPI
BBP4	115.9°± 2.3	126.8°± 2.0	26.2°± 2.7
Sigraflex	95.2°± 2.7°	114.6°± 7.3	27.5°± 3.9°

Table 2

flow field design A = anode C = cathode	method / -	electrode surface / cm^2	land width / mm	channel width / mm	channel height / mm	channel length / mm	sum of channel cross sections / mm^2	area ratio of channel to land / %	flow rate / mm s^{-1}
A-ME15, 6-fold meander	SCT[1]/ NR[2]	314.75	1.0-2.3	1.5	1.5	1523-1596	13.5	44.6	24.16
C-CH15, channel	SCT[1]/ NR[2]	314.75	1.5	1.5	1.5	151	157.5	49.9	368
C-GR10, grid	SCT[1]/ NR[2]	314.75	1.0	1.0	1.0	151	105.0-209.0[3]	74.4	277-552
C-GR15, grid	SCT[1]	314.75	1.5	1.5	1.5	151	157.5-312.75[3]	74.3	185-368

[1] SCR = segmented cell technology, [2] NR = neutron radiography; [3]lower value: grid design, higher value: channel design

material	UNT	HPO	HPI
BBP4	115.9°± 2.3	126.8°± 2.0	26.2°± 2.7
Sigraflex	95.2°± 2.7°	114.6°± 7.3	27.5°± 3.9°